communications physics

A Nature Portfolio journal

Article

https://doi.org/10.1038/s42005-026-02808-z

Control of helix orientation in chiral magnets via lateral confinement

M. Colling[1], M. Stepanova[1], M. Hentschel[2], S. Bhattacharjee[3], E. Lysne[1], K. Hunnestad[1], N. Kanazawa[4], Y. Tokura[5,6,7], J. Masell[3,5] ✉ & D. Meier[1,8,9] ✉

Helimagnetic materials offer a versatile platform for spin-based device concepts owing to their long-range, tunable spiral order. Here, we demonstrate controlled manipulation of the helimagnetic propagation vector $\boldsymbol{q}$ by geometrical confinement, using FeGe as a model Dzyaloshinskii–Moriya interaction (DMI)-driven chiral magnet. Micromagnetic simulations based on the nonlinear sigma model reveal that open boundaries give rise to a chiral surface twist acting as an effective surface anisotropy, which dictates the preferred helix orientation in the absence of magnetostatic shape effects. This geometry-induced anisotropy is quantitatively captured by an analytical model derived from the DMI boundary condition. Magnetic force microscopy measurements on focused-ion-beam structured FeGe confirm the predicted orientation behavior and establish geometry-controlled helimagnetic order as a robust, tunable mechanism for steering DMI-stabilized spin-spiral states. The concept provides a general route toward device-level control of chiral magnetic order in non-centrosymmetric systems.

Ferromagnetic materials form an important foundation for computing technologies, most notably in magnetic memory devices such as magnetic tapes, hard disk drives, and magnetic random-access memory[1–5]. Their clear magnetic contrast and straightforward control have made them indispensable for data storage. However, the strong dipolar stray fields inherent to ferromagnets cause cross-talk between neighboring elements and hinder device miniaturization, posing fundamental limitations for high-density integration and energy-efficient operation. To overcome these drawbacks, antiferromagnets have attracted attention for their compensated spin structure, which eliminates dipolar stray fields and enables ultrafast spin dynamics[6–9]. Yet, the same compensation makes them difficult to manipulate and detect, restricting their direct use in practical devices. Altermagnets have recently been proposed as a symmetry-driven alternative that combines the spin polarization of ferromagnets with the magnetic compensation of antiferromagnets, potentially offering the best of both worlds[10–13].

At the same time, other magnetic materials with more complex spin orders have moved into focus, motivated by their unusual physical properties, which enable innovative approaches for information processing and data storage[14–18]. Among these systems, helimagnets represent an intriguing case: their noncollinear spin order combines characteristics of ferromagnets and antiferromagnets, exhibiting low or vanishing dipolar stray fields while retaining spin dynamics and transport features characteristic of ferromagnets[19–23]. Helimagnetic materials exhibit long-range spiral arrangements of spins characterized by a propagation vector $\boldsymbol{q}$, which defines the direction and periodicity of the helical order, as illustrated in Fig. 1. Depending on the crystal symmetry and intrinsic magnetic anisotropy, $\boldsymbol{q}$ typically aligns along high-symmetry axes in the ground state[24,25]. However, the orientation of $\boldsymbol{q}$ can be altered by external stimuli, such as magnetic fields or electric currents, affecting key physical properties including magnetoresistance and spin-wave propagation[20,26,27]. This tunability, which is leveraged in the emerging field referred to as helitronics, highlights the potential of helimagnetic systems for reconfigurable spin-based devices[28].

Controlling helimagnetic order at the local length scale and in device-relevant confined geometries, however, remains a challenging task. In seminal studies, it was demonstrated that helical spin textures with $\boldsymbol{q}$ parallel to the surface emerge in manganese (Mn) monolayers on W(110)[29,30], whereas in B20 compounds the helix axis in bulk crystals typically follows crystallographic high-symmetry directions with a tendency to align with the

[1]Department of Materials Science and Engineering, Norwegian University of Science and Technology (NTNU), Trondheim, Norway. [2]4th Physics Institute and Research Center SCoPE, University of Stuttgart, Stuttgart, Germany. [3]Institute of Theoretical Solid State Physics, Karlsruhe Institute of Technology, Karlsruhe, Germany. [4]Institute of Industrial Science, University of Tokyo, Tokyo, Japan. [5]RIKEN Center for Emergent Matter Science (CEMS), Wako, Japan. [6]Department of Applied Physics, University of Tokyo, Tokyo, Japan. [7]Tokyo College, University of Tokyo, Tokyo, Japan. [8]Faculty of Physics and Center for Nanointegration Duisburg-Essen (CENIDE), University of Duisburg-Essen, Duisburg, Germany. [9]Research Center Future Energy Materials and Systems, Research Alliance Ruhr, Bochum, Germany. ✉e-mail: jan.masell@kit.edu; dennis.meier@uni-due.de

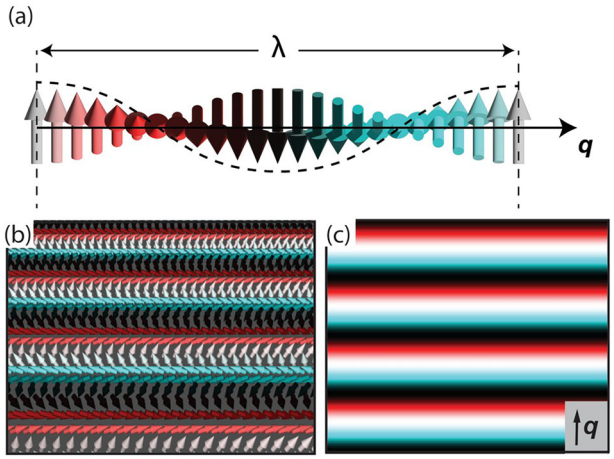

Fig. 1 | Helical spin order in FeGe. a Schematic illustration of the helical ground state showing the wavelength λ and propagation direction $\boldsymbol{q}$. **b** Micromagnetic simulation of the helical state with the magnetization shown as arrows and color-coded according to the local magnetization direction (black = down, white = up, red = right, cyan = left). **c** Corresponding color-map representation of the same state as in (**b**).

surface normal near exposed surfaces and in thin films[29,31–33]. In such confined geometries, additional anisotropies become relevant: in many B20 thin films, shape anisotropy and epitaxial strain favor $\boldsymbol{q}$ along the film normal, whereas at free surfaces of bulk single crystals, surface anisotropies can stabilize an in-plane orientation of $\boldsymbol{q}$[21,31,33,34].

This sensitivity to competing anisotropies highlights the potential for tailoring the helix orientation through geometry, interfaces, and confinement. The examples above illustrate the general impact of geometrical confinement, which can readily be leveraged to control magnetic shape anisotropy and, hence, the propagation direction of the helimagnetic order.

In contrast to vertical confinement effects in thin-film structures, where thickness has been shown to alter the orientation and stability of helical states[35], the effect of lateral confinement in helimagnets is much less explored. Existing work on nanostructured chiral magnets has predominantly focused on skyrmionic textures in confined geometries, such as FeGe nanodisks[36,37], Fe/Ir(111) islands[38], patterned "geometric corrals"[39], and FeGe nanostripes[40,41]. While these studies primarily address skyrmions, they also reveal that the underlying helical state is strongly affected by lateral confinement—influencing stability ranges, domain formation, and boundary behavior. Indeed, understanding how confinement modifies the spin helix is also crucial for controlling skyrmions, as the skyrmion phase often emerges from, or coexists with, the helical phase.

Here, we study the impact of lateral confinement on the helimagnetic order in FeGe. Using micromagnetic simulations, we calculate the helimagnetic order in rectangular specimens of varying aspect ratio, determining the energy landscape and the resulting $\boldsymbol{q}$-vector orientation. Complementary magnetic force microscopy (MFM) measurements on comparable patterns at the surface of an FeGe single crystal corroborate the simulation results, showing a substantial effect of the lateral confinement even when the helical spin textures are not fully decoupled from the magnetic order in the bulk. Our results give additional insights into helimagnetism in geometrically confined spaces and general guidelines for property engineering.

Helical order under lateral confinement

FeGe naturally forms a helical spin structure below $T_c \approx 278$ K with a wavelength $\lambda \approx 70$ nm [24,25]. The system belongs to the non-centrosymmetric B20 family and has attracted broad attention as a high-temperature skyrmion host material[42–45] and a platform for studying topological dislocations and domain walls[21,34,46,47]. Importantly for this work, its helimagnetism and fundamental physical properties are well characterized[24,35,42,48,49], making FeGe an ideal model system for investigating lateral confinement effects. In bulk single crystals, $\boldsymbol{q}$ first aligns along ⟨100⟩ crystallographic directions close to T_c and switches to ⟨111⟩ directions upon cooling, whereas at the surface an in-plane orientation of $\boldsymbol{q}$ is generally favored [21,25,34]. Aside from this surface anchoring, the in-plane orientation of $\boldsymbol{q}$ in FeGe has been shown to be nearly isotropic[21,34], with the cubic magnetocrystalline anisotropy being weak near T_c[25]. Consistent with literature[27,28], we therefore model the surface order observed by MFM as an isotropic two-dimensional system, where the bulk's cubic magnetocrystalline anisotropy is neglected.

Anisotropy due to chiral surface twist

To model the helimagnetic order in FeGe and calculate the energetics, we apply a similar micromagnetic model as in previous studies[37,50] (see Supplementary Information for details). The model includes the standard magnetic stiffness A_{ex} and bulk-type Dzyaloshinskii-Moriya interaction (DMI) D, see Supplementary Eq. (S1). The parameters are chosen to reproduce the experimentally observed helical wavelength of $\lambda \approx 70$ nm and the critical field for the conical–polarized transition in bulk FeGe. Magnetostatic interactions are omitted because (i) the Bloch-type windings in the bulk produce no magnetic volume charges, $\nabla \cdot \boldsymbol{m}$, and therefore no demagnetizing field, and (ii) the surface charges, $\hat{\boldsymbol{n}} \cdot \boldsymbol{m}$, while nonzero, are negligible in the DMI-dominated regime relevant here (see Supplementary Note 2F). No additional magnetic anisotropy terms are included. Simulations are performed using an enhanced version of MUMAX3[51,52], which implements higher-order finite-difference stencils to minimize artificial anisotropies originating from the discretization. Lateral confinement is modeled by simulating rectangular specimens of varying aspect ratios with open boundary conditions, using a single discretization cell along the thickness direction to effectively represent a two-dimensional system. System sizes are selected to minimize commensurability artifacts between the simulated geometry and the helical wavelength.

We first analyze magnetic anisotropy in a rectangular test structure (aspect ratio 2:1), as shown in Fig. 2. Figure 2a shows a ferromagnet with long-range dipolar interactions, simulated in a 560 nm × 280 nm ($8\,\lambda \times 4\,\lambda$) rectangular geometry using our customized FeGe parameters, including the demagnetizing field but no DMI. During energy minimization, specific trial orientations of the magnetization, $\boldsymbol{M}$, in the sample interior were fixed, while only the outer region was allowed to relax. As expected for conventional ferromagnetic order, in this configuration, $\boldsymbol{M}$ aligns preferentially along the long side of the rectangle and remains confined to the sample plane as a direct consequence of shape anisotropy.

In Fig. 2b, we show the helimagnetic order that arises when switching on the DMI but neglecting dipolar interactions. In this scenario, the associated propagation vector, $\boldsymbol{q}$, aligns along the diagonal, which reduces the total edge energy by orienting the helical stripes so that both sample edges contribute equally to the boundary-induced spin rotation. This phenomenon is known as chiral surface twist[53–55]. The surface twist lowers the energy for certain helix orientations relative to the boundary and thus acts as an effective surface anisotropy (see boundary condition in Eq. (1)). The comparison of Fig. 2a and b highlights a qualitatively different response to shape anisotropy: alignment of $\boldsymbol{M}$ with the long outer axis for the ferromagnet versus a diagonal orientation of $\boldsymbol{q}$ for the helimagnet.

A more detailed analysis of the two systems is displayed in Fig. 2c (ferromagnet: gray dots; helimagnet: black dots), showing the energy as a function of the orientation angle, θ, defined in Figs. 2a,b. For the helimagnet, the values are obtained by preparing helical states of the ideal wavelength, relaxing the edges, and optimizing the spatial phase shift, ϕ, which describes the translation of the helix along the $\boldsymbol{q}$-vector. The residual oscillations arise from edge-related commensurability effects. Both systems exhibit distinct angular dependencies, with minima at $\theta = 13^\circ$ (ferromagnet) and $\theta = 30^\circ$ (helimagnet), marked by orange stars. For the ferromagnet, the minimum is slightly offset from $\theta = 0^\circ$ due to a small tilt of $\boldsymbol{M}$ near the edges. By symmetry, the energy curves are mirror-symmetric about 0° and 90° and periodic with a periodicity of 180°.

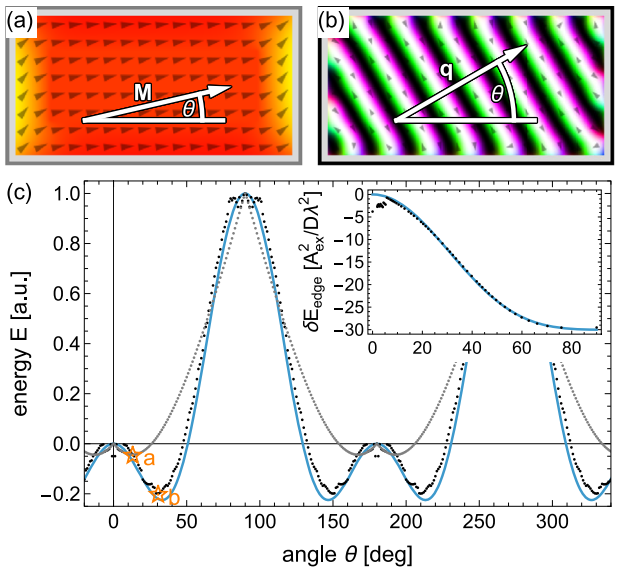

Fig. 2 | Shape anisotropy in a rectangular magnet with an aspect ratio of 2:1. **a** Simulated ferromagnetic state including dipolar interactions, showing alignment of $\boldsymbol{M}$ along the long axis due to conventional shape anisotropy. Color denotes the orientation of the magnetization, see Fig. 1, with gray triangles emphasizing the in-plane orientation. The large white arrow highlights the orientation of the magnetization in the middle of the sample and its angle θ with the x-axis. **b** Simulated helical state without demagnetization energy, where the propagation vector $\boldsymbol{q}$ aligns diagonally to minimize the boundary energy through the chiral surface twist. Color scheme as in (**a**), with the large white arrow indicating the orientation of the $\boldsymbol{q}$-vector in the middle of the sample. **c** Corresponding energy landscapes as a function of orientation angle θ. Orange stars mark the energy minima. In the main panel, the blue line is the analytical result of Eq. (3), obtained by summing the surface-twist energy over the four edges of the rectangle. The inset shows the calculated surface-twist contribution, with the blue line given by the analytical harmonic model of Eq. (2).

As already noted, for chiral magnets described by Supplementary Eq. (S1), the boundary condition[53,54]

$$\partial_n \boldsymbol{m} = \frac{D}{2A_{ex}}\, \boldsymbol{n}\times\boldsymbol{m} \tag{1}$$

enforces a rotation of the local magnetization $\boldsymbol{m}$ about the surface normal $\boldsymbol{n}$ on the length scale $\frac{2A_{ex}}{D} = \frac{\lambda}{2\pi} = \frac{1}{|\boldsymbol{q}|}$. This condition is trivially fulfilled for $\boldsymbol{q}\|\boldsymbol{n}$, whereas for other orientations of $\boldsymbol{q}$ the energy can be lowered by additional twisting at the surface. We numerically calculate this energy gain per surface area δE_{edge}, which is shown in the inset of Fig. 2c as black dots, displayed in dimensionless units using the energy $\frac{A_{ex}^2}{D}$ per area λ^2 (see Supplementary Note 2A). The result is a smooth curve for $\theta \gtrsim 6^\circ$ with a shallow minimum around $\theta = 90^\circ$. In turn, for $\theta \lesssim 6^\circ$, the projected helical wavelength diverges and the helical state becomes almost translation invariant along the edge. This invariance is broken by an energetically favorable surface state with additional twisting along the edge, referred to as stacked spirals in literature[56]. Real-space figures of these special states are included in Supplementary Fig. S1.

Neglecting the range $\theta \lesssim 6^\circ$ where non-linear surface reconstruction sets in, the angular dependence is well described by the lowest-order symmetry-allowed harmonics (see Supplementary Note 2A),

$$\frac{\delta E_{\text{edge}}}{\frac{A_{ex}^2}{D}/\lambda^2} = c_2 \sin^2\theta + c_4 \sin^4\theta. \tag{2}$$

Note that the zeroth-order contribution (constant offset) precisely vanishes due to the above argument that a helix with $\boldsymbol{q}\|\boldsymbol{n}$ could stay pristine and would not gain any energy. Fitting Eq. (2) to our numerical data in the inset of Fig. 2c, we find $c_2 \approx -55$ and $c_4 \approx 25$, which is independent of the micromagnetic constants as the problem is dimensionless. For these parameters, the harmonic surface energy function, Eq. (2), is shown as the blue line in Fig. 2c, matching the numerical data for $\theta \gtrsim 6^\circ$. Furthermore, we use the expression in Eq. (2) to estimate the energy as a function of the $\boldsymbol{q}$-vector orientation in a more complex geometry, here the rectangular sample in Fig. 2b. The resulting function, displayed as the blue line in the main panel of Fig. 2c, reproduces the numerical data, including the energy minimum, and only minor commensurability-related oscillations are not captured.

In conclusion, the combined numerical and analytical analyses demonstrate that the chiral surface twist constitutes an effective surface anisotropy, that governs the preferred helix orientation in confined geometries.

Shape anisotropy of the helix

Next, we vary the width L_x and height L_y of our FeGe model system to investigate how the aspect ratio affects the energy landscape.

Figure 3a summarizes the energetically most favorable angles θ, i.e., the angles between $\boldsymbol{q}$ and $\hat{e}_x$, as function of both L_x and L_y. Note that in contrast to the previous section, we do not pin any parts of the magnetic texture during minimization, so that the helimagnetic texture can freely adapt its orientation to minimize the energy. Selected examples for the lowest energy states are shown in Fig. 3b, marked by black squares in Fig. 3a.

We find that the phase diagram, Fig. 3a, is symmetric around $L_x = L_y$, with an exception at $(1.5\lambda, 1.5\lambda)$ where the system is too small and a state with spontaneously broken symmetry emerges. For sufficiently elongated samples, $\boldsymbol{q}$ aligns parallel to the longer axis (dark red/blue), in agreement with previous observations on highly elongated FeGe nanostripes[40,41], rotating almost monotonously and smoothly as the aspect ratio varies between the two end states. It is important to note, however, that within the sample, the helical orientation is not homogeneous and can significantly vary near the edges and corners as seen in Fig. 3b.

Finally, we compare the results of the numerical minimization to the analytical model in Eq. (2). The energy of the chiral surface twist is given by

$$E_{\text{tot}}/d = 2L_y\, \delta E_{\text{edge}}(\theta) + 2L_x\, \delta E_{\text{edge}}(\theta + \pi/2) \tag{3}$$

where d is the sample thickness. After some algebra, see Supplementary Note 2B, and exploiting that θ depends only on the ratio $R = L_x/L_y$ and the ratio $c = 2c_4/c_2$, we obtain the result

$$\theta = \arctan\left[\sqrt{\frac{(c+1)R-1}{c-R+1}}\right]. \tag{4}$$

In this expression, the fit factor $c \approx -50/55$ is obtained from fitting the data in the inset of Fig. 2, as described above. We show the analytical result together with the full numerical data in Fig. 3c. The agreement is good and particularly accurate for larger systems, here quantified by a greater circumference, $2L_x + 2L_y$, which are less affected by commensurability effects at the corners. We discuss in Supplementary Note 2E that this approach is also valid for other types of polygonal shapes. Figure 3c also includes experimental results, indicated by a red star and red squares with error bars, which are in good agreement with the theoretical prediction. The experimental tests from which the data points are derived are the subject of the following section.

Experimental results

To demonstrate the general possibility of controlling helimagnetism in laterally confined structures experimentally and verify the simulation results

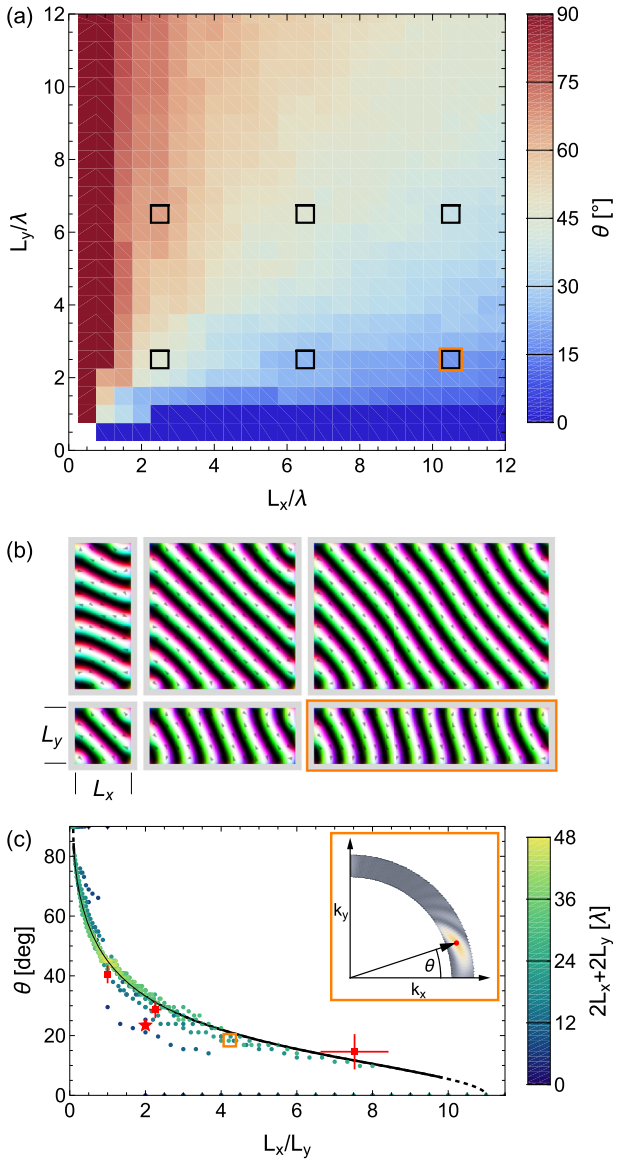

Fig. 3 | Dependence of the helix orientation on the aspect ratio of the confined region. a Color-coded phase diagram of the equilibrium orientation angle θ between $\boldsymbol{q}$ and $\hat{e}_x$, plotted as a function of lateral dimensions L_x and L_y. Blue and red correspond to $\theta = 0^\circ$ and 90°, respectively. Black squares mark data points for which the corresponding real-space textures are shown in (**b**). **b** Representative relaxed helical states for selected aspect ratios. **c** Orientation angle θ as a function of the aspect ratio L_x/L_y. Dots show numerical results colored by the total circumference; the black line represents the analytical model derived from the DMI boundary condition. Dashed segments denote the range outside the model's validity ($6^\circ \lesssim \theta \lesssim 84^\circ$). The inset illustrates the restricted Fourier transform used to extract θ, shown here for $(L_x, L_y) = (10.5\lambda, 2.5\lambda)$, corresponding to the orange box in(**a**, **b**).

based on a real physical material, we conduct different experiments on FeGe lamellas and nano-structured single crystals. Figure 4 summarizes the results gained on a FeGe lamella that was cut from a single crystal using a focused ion beam (FIB, see Methods). A scanning electron microscopy (SEM) image of the lamella is presented in Fig. 4a (thickness ≈ 1 μm). A representative MFM image recorded at $T = 261$ K in the area marked by the blue square in Fig. 4a is displayed in Fig. 4b. The image is taken in dual-pass MFM mode using a magnetized probe tip (PPP-MFMR by Nanosensors) and shows the characteristic pattern of bright and dark lines associated with the in-plane oriented spin helix in FeGe as explained in detail elsewhere[21]. The MFM image shows that the stripe-like pattern is not parallel to either of the sides of the lamella, exhibiting a nonzero angle θ between the propagation vector $\boldsymbol{q}$ and the positive x-axis (i.e., the long side of the lamella). Based on the Fast Fourier transformation (FFT) of the MFM signal (Fig. 4c), we determine $\theta = 23.7 \pm 1.4^\circ$. This value is in reasonable agreement with the theoretically expected angle $\theta = 33^\circ$ for a sample with aspect ratio 2:1, taking into account the much larger lateral dimension of the lamella for which confinement effects play a less important role than for smaller structures, but cubic anisotropies of the bulk may be more relevant. Independent of this discrepancy, this leads to two important conclusions: (i) the applied nanostructuring process by FIB preserves the helimagnetic texture and (ii) similar to the bulk single crystal from which the lamella was cut, $\boldsymbol{q}$ consistently orients within the surface plane, which is essential for its control via lateral confinement.

In the next step, we move to smaller length scales where confinement is expected to play a more important role and investigate the orientation of the spin helix in different rectangular regions with varying aspect ratios. For this purpose, we use FIB to cut trenches with a depth of about 150 nm into the surface of an FeGe single crystal, creating laterally confined regions with aspect ratios of about 1:1, 2:1, and 7:1. Although in this architecture the magnetic order in the confined structures is not decoupled from the underlying bulk, it has the advantage, compared to the lamella-based experiment, that the surface of interest has not been cut by the ion beam, reducing the risk of extrinsic defect-related pinning effects. Furthermore, right after cutting the trenches, the surface is protected by an ALD-deposited Al_2O_3 capping layer (see Supplementary Fig. S5), which protects the surface from oxidation, giving stable MFM contrast on FeGe on the timescale of months (for comparison, without capping, we observe that the MFM contrast rapidly decays and vanishes after a few days).

The experimental results are presented in Fig. 5, which shows overlays of SEM and MFM images recorded from different rectangles cut into the surface of the same FeGe single crystal. The FIB-cut trenches are visible in the SEM data as darker channels with a width of about 200 nm and the MFM scans reveal the orientation of $\boldsymbol{q}$ with the confined structures as well as in adjacent test regions that are displayed for comparison. To determine the local orientation of $\boldsymbol{q}$, we consider the FFT of the MFM signals, analogous to Fig. 4, as exemplified for two selected regions in Fig. 5a. Based on this analysis, we find the following angles θ between the propagation vector $\boldsymbol{q}$ and the positive x-axis, that is, $40.5 \pm 2.7^\circ$, $28.7 \pm 2.6^\circ$, and $14.6 \pm 5.6^\circ$ for aspect ratios of about 1:1, 2:1, and 7:1, respectively.

For a direct comparison with the theoretically predicted values, the measured angles, together with their uncertainties, are plotted in red in Fig. 3c, showing a remarkable agreement, taking into account that the laterally confined regions are not decoupled from the underlying bulk and its magnetic order. The latter has a different orientation than the helimagnetic order within the rectangles, which is confirmed by the MFM data taken in adjacent regions (see Fig. 5a-c). Notably, in all three cases, the orientation outside the confined regions differs by up to 20° from the inside. The latter reflects that the $\boldsymbol{q}$ orientation is given by the helimagnetic domain orientation of the bulk, which is not controlled by geometry and can vary from region to region. Variations in the exterior angles, such as the difference between the upper (31°) and lower (41°) regions in Fig. 5a, thus naturally occur. Importantly, inside the confined regions, the $\boldsymbol{q}$ orientation consistently follows the predicted geometry dependence, regardless of the exterior orientation. This observation corroborates that the lateral confinement provides a powerful handle for controlling the orientation of the helimagnetic order.

Summary and conclusion

In this work, we demonstrate that lateral confinement provides a robust and tunable handle to control the helimagnetic order in chiral magnets. Using FeGe as a model system, micromagnetic simulations based on the nonlinear sigma model reveal that open boundaries generate a chiral surface twist acting as an effective surface anisotropy, which governs the orientation of the helical propagation vector $\boldsymbol{q}$ in the absence of magnetostatic shape effects. The resulting

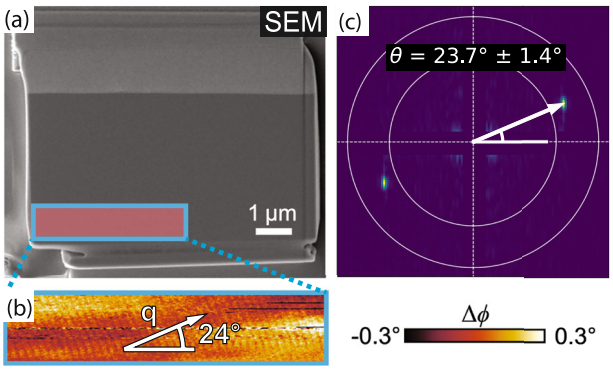

Fig. 4 | Experimental observation of helimagnetic order under lateral confinement. a SEM image of a 1 μm thick FeGe lamella with an aspect ratio of approximately 2:1. **b** Corresponding MFM image revealing helimagnetic order, with propagation vector $\boldsymbol{q}$ tilted relative to the long axis. **c** Fast Fourier transform (FFT) of the MFM image used to determine the orientation angle θ between $\boldsymbol{q}$ and the long axis, yielding 23.7 ± 1. 4°.

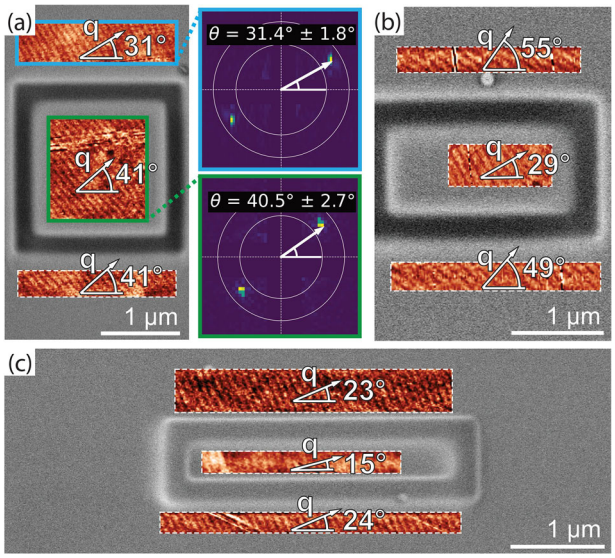

Fig. 5 | Influence of lateral confinement on the helix orientation. a-c SEM images of rectangular FIB-cut regions with aspect ratios of about 1:1, 2:1, and 7:1, respectively. Overlaid MFM scans show the corresponding helimagnetic stripe patterns. White arrows indicate the direction of the helical propagation vector $\boldsymbol{q}$ inside each confined region and the extracted orientation angle θ relative to the long side of the rectangle. The comparison between interior and exterior orientations demonstrates the predictable geometry-dependent reorientation of $\boldsymbol{q}$ in agreement with the simulation results.

geometry-dependent anisotropy leads to a continuous evolution of the preferred helix orientation with the sample aspect ratio, fully captured by an analytical model derived from the DMI boundary condition which is valid for rectangular geometries and beyond.

MFM measurements on laterally confined structures cut into the surface of an FeGe single crystal confirm these predictions and demonstrate their applicability to real physical systems with the experimentally observed helix orientations inside laterally confined regions quantitatively following the simulated orientations. Together, these results establish geometry-induced anisotropy as a general mechanism for steering DMI-driven spin-spiral states, providing a direct route toward device-level control of chiral magnetic order. The concept is universal to DMI-dominated helimagnets and can be extended to multilayer systems and synthetic chiral heterostructures where geometry and boundaries define the local anisotropy landscape. Additional effects are expected to arise in systems with pronounced dipolar interactions (see Supplementary Fig. S4), giving further yet-to-be-explored opportunities for controlling the helimagnetic order.

Methods

Micromagnetic simulations

Micromagnetic simulations were performed using an enhanced version of MUMAX3 (version 3.10) with higher-order finite-difference derivatives to suppress numerical anisotropies. Verification of the higher-order stencil implementation will be published in a separate paper when the feature is made available in the next release of MUMAX3. The numerical discretization is $a = \lambda/32 = 2.1875$ nm. The micromagnetic model and material parameters are given in Supplementary Note 1.

Sample growth

FeGe single crystals were grown by chemical vapor transport using FeGe B35 powder and I_2 as the transport agent. The material was sealed in an evacuated quartz ampoule and heated for 1 month in a three-zone furnace with a temperature gradient of 560 °C to 500 °C, yielding B20 FeGe crystals, typically $0.5 \times 1 \times 1$ mm^3. The B20 structure was confirmed by powder X-ray diffraction.

Sample preparation and nanostructuring

Surface oxide layers were removed by argon ion beam etching (Technics Plasma R.I.B. Etch 160). The desired structures were then patterned into the FeGe surface using focused-ion-beam milling with singly charged gold ions at 35 kV (Raith ionLine). After nanostructuring, the samples were coated with a 5 nm Al_2O_3 layer deposited by ALD (Picosun R-200 Advanced) to prevent surface oxidation.

Magnetic force microscopy measurements

MFM measurements were performed with magnetically coated PPP-MFMR tips in two-pass mode, using the second pass to detect the magnetic signal at a lift height of approximately 30 nm. Imaging was carried out in an NT-MDT scanning probe microscope equipped with a temperature-controlled sample holder, enabling measurements down to 260 K. All experiments were performed in a dry nitrogen environment to ensure stable imaging conditions.

Data availability

The data and simulation scripts that support the findings of this study are openly available in the Zenodo public repository at https://doi.org/10.5281/zenodo.20155860.

Received: 20 January 2026; Accepted: 31 July 2026;
Published online: 01 September 2026

References

1. Wallace Jr, R. L. The reproduction of magnetically recorded signals. *Bell Syst. Tech. J.* **30**, 1145–1173 (1951).
2. Chappert, C., Fert, A. & Van Dau, F. N. The emergence of spin electronics in data storage. *Nat. Mater.* **6**, 813–823 (2007).
3. Parkin, S. S. P., Hayashi, M. & Thomas, L. Magnetic domain-wall racetrack memory. *Science* **320**, 190–194 (2008).
4. Bhatti, S. et al. Spintronics-based random access memory: a review. *Mater. Today* **20**, 530–548 (2017).
5. Bhushan, B. Historical evolution of magnetic data storage devices and related conferences. *Microsyst. Technol.* **24**, 4423–4436 (2018).
6. Jungwirth, T., Marti, X., Wadley, P. & Wunderlich, J. Antiferromagnetic spintronics. *Nat. Nanotechnol.* **11**, 231–241 (2016).
7. Baltz, V. et al. Antiferromagnetic spintronics. *Rev. Mod. Phys.* **90**, 015005 (2018).
8. Jungwirth, T. et al. The multiple directions of antiferromagnetic spintronics. *Nat. Phys.* **14**, 200–203 (2018).

9. Jungfleisch, M. B., Zhang, W. & Hoffmann, A. Perspectives of antiferromagnetic spintronics. *Phys. Lett. A* **382**, 865–871 (2018).
10. Šmejkal, L., Sinova, J. & Jungwirth, T. Emerging research landscape of altermagnetism. *Phys. Rev. X* **12**, 040501 (2022).
11. Song, C. et al. Altermagnets as a new class of functional materials. *Nat. Rev. Mater.* **10**, 473–485 (2025).
12. Song, Q. et al. Electrical switching of a p-wave magnet. *Nature* **642**, 64–70 (2025).
13. Yamada, R. et al. A metallic p-wave magnet with commensurate spin helix. *Nature* **646**, 837–842 (2025).
14. Bramwell, S. T. & Gingras, M. J. P. Spin ice state in frustrated magnetic pyrochlore materials. *Science* **294**, 1495–1501 (2001).
15. Mühlbauer, S. et al. Skyrmion lattice in a chiral magnet. *Science* **323**, 915–919 (2009).
16. Balents, L. Spin liquids in frustrated magnets. *Nature* **464**, 199–208 (2010).
17. Xu, S.-Y. et al. Discovery of a Weyl fermion semimetal and topological Fermi arcs. *Science* **349**, 613–617 (2015).
18. Gong, C. et al. Discovery of intrinsic ferromagnetism in two-dimensional van der Waals crystals. *Nature* **546**, 265–269 (2017).
19. Bogdanov, A. N. & Yablonskii, D. Thermodynamically stable "vortices" in magnetically ordered crystals. the mixed state of magnets. *Zh. Eksp. Teor. Fiz.* **95**, 178 (1989).
20. Koralek, J. D. et al. Observation of coherent helimagnons and Gilbert damping in an itinerant magnet. *Phys. Rev. Lett.* **109**, 247204 (2012).
21. Dussaux, A. et al. Local dynamics of topological magnetic defects in the itinerant helimagnet FeGe. *Nat. Commun.* **7**, 12430 (2016).
22. Georgii, R. & Weber, T. The helical magnet mnsi: Skyrmions and magnons. *Quantum Beam Sci.* **3**, 1 (2019).
23. Sirica, N. et al. The nature of ferromagnetism in the chiral helimagnet cr1/3nbs2. *Commun. Phys.* **3**, 65 (2020).
24. Ishikawa, Y., Tajima, K., Bloch, D. & Roth, M. Helical spin structure in manganese silicide MnSi. *Solid State Commun.* **19**, 525–528 (1976).
25. Lebech, B., Bernhard, J. & Freltoft, T. Magnetic structures of cubic FeGe studied by small-angle neutron scattering. *J. Phys. Condens. Matter* **1**, 6105 (1989).
26. Bauer, A. et al. Symmetry breaking, slow relaxation dynamics, and topological defects at the field-induced helix reorientation in mnsi. *Phys. Rev. B* **95**, 024429 (2017).
27. Masell, J., Yu, X., Kanazawa, N., Tokura, Y. & Nagaosa, N. Combining the helical phase of chiral magnets with electric currents. *Phys. Rev. B* **102**, 180402 (2020).
28. Bechler, N. T. & Masell, J. Helitronics as a potential building block for classical and unconventional computing. *Neuromorphic Comput. Eng.* **3**, 034003 (2023).
29. Haze, M., Yoshida, Y. & Hasegawa, Y. Experimental verification of the rotational type of chiral spin spiral structures by spin-polarized scanning tunneling microscopy. *Sci. Rep.* **7**, 13269 (2017).
30. Honolka, J. et al. Spin-spiral state of a mn monolayer on w(110) studied by soft x-ray absorption spectroscopy at variable temperature. *Phys. Rev. B* **103**, 174419 (2021).
31. Karhu, E. A. et al. Helical magnetic order in mnsi thin films. *Phys. Rev. B* **84**, 060404 (2011).
32. Wilson, M. N., Butenko, A. B., Bogdanov, A. N. & Monchesky, T. L. Chiral skyrmions in cubic helimagnet films: the role of uniaxial anisotropy. *Phys. Rev. B* **89**, 094411 (2014).
33. Kanazawa, N. et al. Direct observation of anisotropic magnetic field response of the spin helix in FeGe thin films. *Phys. Rev. B* **94**, 184432 (2016).
34. Schoenherr, P. et al. Topological domain walls in helimagnets. *Nat. Phys.* **14**, 465–468 (2018).
35. Wilhelm, H. et al. Confinement of chiral magnetic modulations in the precursor region of fege. *J. Phys.: Condens. Matter* **24**, 294204 (2012).
36. Beg, M. et al. Ground state search, hysteretic behaviour and reversal mechanism of skyrmionic textures in confined helimagnetic nanostructures. *Sci. Rep.* **5**, 17137 (2015).
37. Beg, M. et al. Dynamics of skyrmionic states in confined helimagnetic nanostructures. *Phys. Rev. B* **95**, 014433 (2017).
38. Hagemeister, J. et al. Skyrmions at the edge: Confinement effects in Fe/Ir(111). *Phys. Rev. Lett.* **117**, 207202 (2016).
39. Matsumoto, T. & Shibata, N. Confinement of magnetic skyrmions to corrals of artificial surface pits with complex geometries. *Front. Phys.* **9** (2022).
40. Du, H. et al. Edge-mediated skyrmion chain and its collective dynamics in a confined geometry. *Nat. Commun.* **6**, 8504 (2015).
41. Jin, C. et al. Control of morphology and formation of highly geometrically confined magnetic skyrmions. *Nat. Commun.* **8**, 15569 (2017).
42. Yu, X. Z. et al. Near room-temperature formation of a skyrmion crystal in thin-films of the helimagnet FeGe. *Nat. Mater.* **10**, 106–109 (2011).
43. Huang, S. X. & Chien, C. L. Extended skyrmion phase in epitaxial FeGe(111) thin films. *Phys. Rev. Lett.* **108**, 267201 (2012).
44. Legrand, W. et al. Room-temperature current-induced generation and motion of sub-100 nm skyrmions. *Nano Lett.* **17**, 2703–2712 (2017).
45. Leroux, M. et al. Skyrmion lattice topological Hall effect near room temperature. *Sci. Rep.* **8**, 15510 (2018).
46. Schoenherr, P. et al. Dislocation-driven relaxation processes at the conical to helical phase transition in FeGe. *ACS Nano* **15**, 17508–17514 (2021).
47. Stepanova, M. et al. Detection of topological spin textures via nonlinear magnetic responses. *Nano Lett.* **22**, 14–21 (2021).
48. Turgut, E. et al. Chiral magnetic excitations in FeGe films. *Phys. Rev. B* **95**, 134416 (2017).
49. Wang, K., Wei, W. & Du, H. The cubic b20 chiral magnet fege. *Adv. Funct. Mater.* **35**, 2416203 (2025).
50. Rybakov, F. N., Borisov, A. B. & Bogdanov, A. N. Three-dimensional skyrmion states in thin films of cubic helimagnets. *Phys. Rev. B* **87**, 094424 (2013).
51. Vansteenkiste, A. et al. The design and verification of mumax3. *AIP Adv.* **4**, 107133 (2014).
52. Exl, L. et al. LaBonte's method revisited: an effective steepest descent method for micromagnetic energy minimization. *J. Appl. Phys.* **115**, 17D118 (2014).
53. Rohart, S. & Thiaville, A. Skyrmion confinement in ultrathin film nanostructures in the presence of Dzyaloshinskii-Moriya interaction. *Phys. Rev. B* **88**, 184422 (2013).
54. Meynell, S. A., Wilson, M. N., Fritzsche, H., Bogdanov, A. N. & Monchesky, T. L. Surface twist instabilities and skyrmion states in chiral ferromagnets. *Phys. Rev. B* **90**, 014406 (2014).
55. Müller, J., Rosch, A. & Garst, M. Edge instabilities and skyrmion creation in magnetic layers. *N. J. Phys.* **18**, 065006 (2016).
56. Rybakov, F. N., Borisov, A. B., Blügel, S. & Kiselev, N. S. New spiral state and skyrmion lattice in 3d model of chiral magnets. *N. J. Phys.* **18**, 045002 (2016).

Author contributions

M.C. wrote the manuscript and prepared Figs. 1, 4, and 5 under the supervision of D.M. J.M. wrote and tested the modified micromagnetic simulation framework. J.M. and S.B. performed the micromagnetic simulations, analyzed the data, derived the analytical theory, and prepared Figs. 2 and 3. M.S. and E.L. carried out the MFM measurements. M.H. nanostructured and prepared the samples. K.H. performed the SEM imaging. N.K. and Y.T. provided the FeGe single crystals. All authors discussed the results and contributed to the final version of the manuscript.

Funding

M.C. and D.M. acknowledge funding from the European Union's Horizon Europe Programme Horizon.1.2 under the Marie Skłodowska-Curie Actions

(MSCA), Grant agreement No. 101119608 (TOPOCOM). M.S., E.L., and D.M. acknowledge funding from the Research Council of Norway, project number 263228, and support through the Norwegian Micro- and Nano-Fabrication Facility, NorFab (project number 295864). M.S., E.L., and D.M. acknowledge support by the Research Council of Norway through its Centres of Excellence funding scheme, Project No. 262633, "QuSpin". D.M. thanks NTNU for support via the Onsager Fellowship Program and the Outstanding Academic Fellows Program. J.M. and S.B. acknowledge funding from the Deutsche Forschungsgemeinschaft (DFG, German Research Foundation) under the Project No. 547968854. Open access funding provided by NTNU Norwegian University of Science and Technology (incl St. Olavs Hospital - Trondheim University Hospital).

Competing interests

The authors declare no competing interests.

Additional information

Supplementary information The online version contains supplementary material available at https://doi.org/10.1038/s42005-026-02808-z.

Correspondence and requests for materials should be addressed to J. Masell or D. Meier.

Peer review information *Communications Physics* thanks Jan Honolka and the other, anonymous, reviewer for their contribution to the peer review of this work.